



Contents lists available at ScienceDirect

Journal of Marine Systems

journal homepage: [www.elsevier.com/locate/jmarsys](http://www.elsevier.com/locate/jmarsys)

# Comparison between a reanalyzed product by 3-dimensional variational assimilation technique and observations in the Ulleung Basin of the East/Japan Sea

Young Ho Kim <sup>a,\*</sup>, Kyung-Il Chang <sup>b</sup>, Jong Jin Park <sup>c</sup>, Seon Ki Park <sup>d</sup>, Sang-Hyun Lee <sup>b</sup>, Young-Gyu Kim <sup>e</sup>,  
Kyung Tae Jung <sup>a</sup>, Kuh Kim <sup>b</sup>

<sup>a</sup> Coastal Engineering Research Department, Korea Ocean Research and Development Institute, Ansan P.O. Box 29, Seoul 425-600, South Korea

<sup>b</sup> Research Institute of Oceanography/School of Earth and Environmental Sciences, Seoul National University, Seoul 151-742, South Korea

<sup>c</sup> Woods Hole Oceanographic Institution, Woods Hole, MA02543, USA

<sup>d</sup> Severe Storm Research Center and Dept. of Environmental Sci. & Eng., Ewha Womans University, Seoul 120-750, South Korea

<sup>e</sup> Agency for Defense Development, P.O. Box 18, Chinhae 645-600, South Korea

## ARTICLE INFO

### Article history:

Received 18 June 2007

Received in revised form 19 November 2007

Accepted 26 February 2009

Available online xxx

### Keywords:

Modeling

Oceanic currents

Oceanic eddies

3-dimensional variational technique

East Sea Regional Ocean Model

North Korean Cold Current

East/Japan Sea

Ulleung Basin

## ABSTRACT

Reanalyzed products from a MOM3-based East Sea Regional Ocean Model with a 3-dimensional variational data assimilation module (DA-ESROM), have been compared with the observed hydrographic and current datasets in the Ulleung Basin (UB) of the East/Japan Sea (EJS). Satellite-borne sea surface temperature and sea surface height data, and temperature profiles have been assimilated into the DA-ESROM. The performance of the DA-ESROM appears to be efficient enough to be used in an operational ocean forecast system. Comparing with the results from Mitchell et al. [Mitchell, D. A., Watts, D. R., Wimbush, M., Teague, W.J., Tracey, K. L., Book, J. W., Chang, K.-I., Suk, M.-S., Yoon, J.-H., 2005a. Upper circulation patterns in the Ulleung Basin. Deep-Sea Res. II, 52, 1617–1638.], the DA-ESROM fairly well simulates the high variability of the Ulleung Warm Eddy and Dok Cold Eddy as well as the branching of the Tsushima Warm Current in the UB. The overall root-mean-square error between 100 m temperature field reproduced by the DA-ESROM and the observed 100-dbar temperature field is 2.1 °C, and the spatially averaged grid-to-grid correlation between the two temperature fields is high with a mean value of 0.79 for the inter-comparison period. The DA-ESROM reproduces the development of strong southward North Korean Cold Current (NKCC) in summer consistent with the observational results, which is thought to be an improvement of the previous numerical models in the EJS. The reanalyzed products show that the NKCC is about 35 km wide, and flows southward along the Korean coast from spring to summer with maximum monthly mean volume transport of about 0.8 Sv in August–September.

© 2009 Elsevier B.V. All rights reserved.

## 1. Introduction

With an increase in computing power as well as accumulation of data via satellites and various observation programs worldwide concern on development of ocean forecast systems has grown over the last decade (Baharel et al., 2006; Bell et al., 2006). A prerequisite of the forecast system development is to devise a data assimilation technique for the model initialization with a sufficient amount of data available for the data assimilation. The East/Japan Sea (EJS) has recently received considerable attention partly because a substantial amount of data has been accumulated through regular and intense observation programs and partly because, in spite of its relative smallness in size, the typical oceanic features in circulation and hydrography such as western boundary currents and sub-polar front exist as noted by Ichiye and Takano (1988).

The EJS is a semi-enclosed marginal sea surrounded by Korea, Japan and Russia (Fig. 1). While the maximum depth of the EJS reaches 4000 m, exchanges of water mass with the neighboring seas occur through the four shallow straits less than 200 m (see Na et al., this issue). The EJS consists of three basins, the Ulleung Basin (UB) to the southwest with a maximum water depth of about 2300 m connected with the Korea Strait, the Japan Basin occupying the northern half of the EJS with a maximum water depth of about 4000 m, and the Yamato Basin to the southeast with a maximum water depth of about 2700 m.

The Tsushima Warm Current (TWC) entering into the UB through the Korea Strait separates into two or three branches (Kawabe, 1982a,b; Yoon, 1982a,b). The first one is the Nearshore Branch along the Japanese coast, the second one is the Offshore Branch along the continental slope off the Japanese coast, and the third is the East Korean Warm Current (EKWC) flowing northward along the western boundary of the EJS. In general, the EKWC separates from the boundary between 37°N and 38°N, and flows eastward towards the Tsugaru Strait. One of the noticeable hydrographic features in the UB is that the intermediate cold and less saline water is often observed (Kim and Kim, 1983; Kim and

\* Corresponding author. Tel.: +82 31 400 7697; fax: +82 31 408 5823.

E-mail address: [yhkim@kordi.re.kr](mailto:yhkim@kordi.re.kr) (Y.H. Kim).

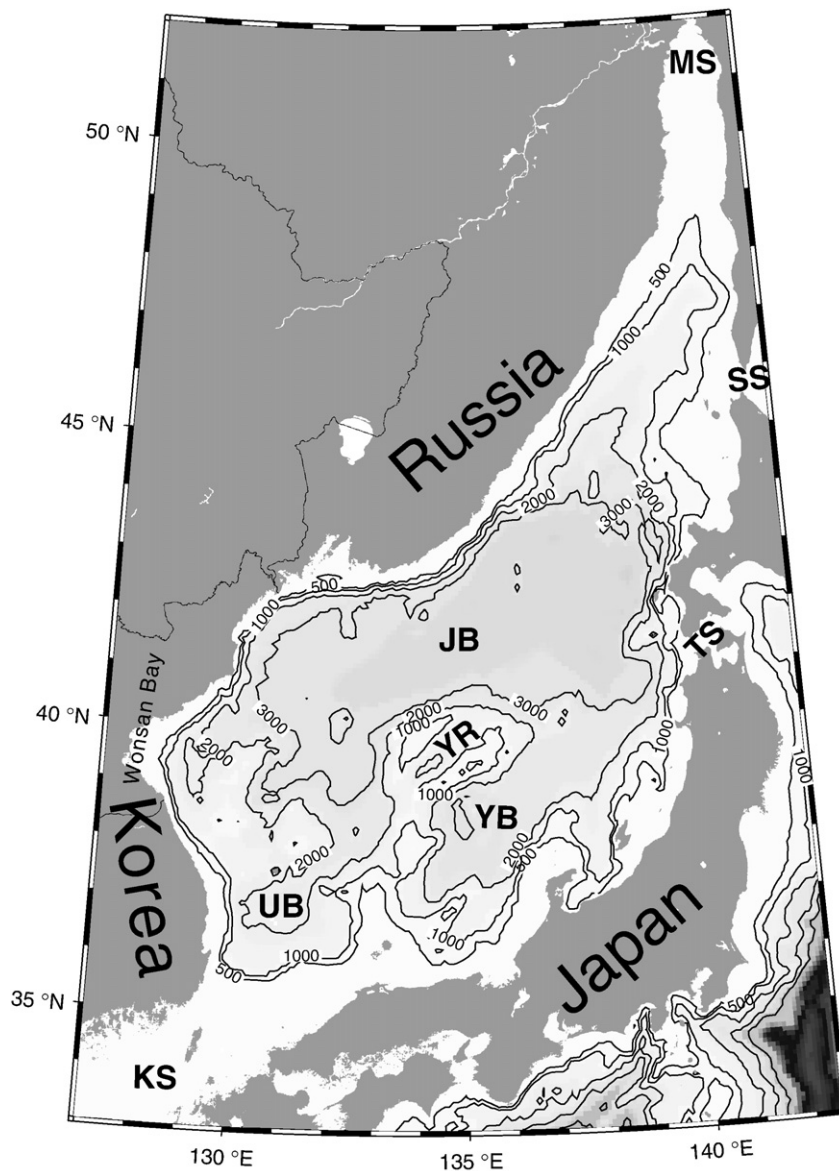


**Fig. 1.** Bathymetry of the East/Japan Sea; UB(Ulleung Basin), YB(Yamato Basin), JB(Japan Basin), YR(Yamato Rise), KS(Korea Strait), TS(Tsugaru Strait), SS(Soya Strait), and MS (Mamiya Strait or Tatar Strait). Thin solid lines represent the bottom contours in meters.

Chung, 1984). Kim and Kim (1983) suggests that the North Korean Cold Water (NKCW), characterized by the salinity minimum layer (SML) and oxygen maximum layer water, flows southward underneath the northward flowing EKWC along the east coast of Korea in summer. In addition, Kim and Chung (1984) found the SML and oxygen maximum layer water in the UB and named it the East Sea Intermediate Water (ESIW). Cho and Kim (1994) suggest that the NKCW and ESIW are two modes of the SML water in the UB. In particular, Cho and Kim (1996) observed the absence of the EKWC in February of 1991 and 1992 and suggested that the NKCW might play a role in the disappearance of the EKWC. A comprehensive review of the hydrography and circulation in the UB can be found in Chang et al. (2005).

The circulation and hydrography in EJS using three-dimensional numerical ocean models have long been investigated by many researchers. Recent numerical model studies in the EJS have successfully reproduced the branching of the TWC and the separation latitude of the EKWC to the south of 38°N (Kim and Yoon, 1999; Yoshikawa et al., 1999; Yoon and Kawamura, 2002; Lee et al., 2003), which corresponds to the observed separation position (Park et al., 2004). In addition, recent high resolution model of 1/36° reproduces meso- and submeso-scale

variabilities in the EJS (Yoon and Kim, 2007-this issue). In spite of this improvement in the surface circulation, the numerical models have not been able to reproduce the intermediate circulation in the UB properly. While most numerical models have a strong southward current, called the North Korean Cold Current (NKCC), in winter, observations showed the appearance of the coldest water (NKCW) carried by the NKCC in summer, implying the strong NKCC along the east coast of Korea. Correspondingly, the SML depth, simulated by numerical models, is often much deeper than the observed depth level.

In all of the above numerical investigations, no data assimilation is applied, except Yoshikawa et al. (1999) who incorporated a simple nudging method into a numerical model. Hirose et al. (1999) applied a data assimilation based on an approximate Kalman Filter to a layered model and Ishikawa et al. (2007-this issue) did a 4-dimensional variational data assimilation to a 3-dimensional ocean circulation model. In this paper, we introduce, as a first step of developing an ocean forecast system, the East Sea Regional Ocean Model (ESROM) with a data assimilation module, and compare the reanalyzed products with available observations for the validation. The 3-dimensional variational assimilation technique has been applied to assimilate the

124 temperature profiles, and satellite-derived sea surface temperature  
125 (SST) and sea surface height anomaly (SSHA) into the ESROM in this  
126 work, which is based on the correlation model by Weaver and Courtier  
127 (2001). For the assimilation of the SSHA, modified Cooper and Haines  
128 (1996)'s method has been used. Details of the ESROM are presented  
129 in Section 2. The data assimilation technique and datasets for the  
130 assimilation are introduced in Section 3, and comparison between the  
131 reanalyzed products and observations follows in Section 4. Finally,  
132 summary and discussion are given in Section 5.

## 133 2. East Sea Regional Ocean Model

134 The ESROM is based on the MOM 3 (Modular Ocean Model version  
135 3, Pacanowski and Griffies, 1999) which is a finite difference model  
136 with the horizontal B-grid and vertical z-coordinate. The MOM 3  
137 adopts the MPI (Message Passing Interface) parallel processing to  
138 reduce computational time, and includes the free surface momentum  
139 equations for the barotropic system (Griffies et al., 2001). The model  
140 solves the three dimensional ocean primitive equations with the  
141 hydrostatic and Boussinesq approximations.

142 While the centered scheme is employed for the momentum  
143 advection, the second-order moment (SOM) advection scheme  
144 (Prather, 1986) is adopted for the tracer advection of the ESROM. In  
145 general, the SOM advection scheme improves tracer distributions  
146 and transports compared to FCT (flux corrected transport) and  
147 QUICKER (quadratic upstream interpolation for convective kine-  
148 matics) schemes (Hofmann and Maqueda, 2006).

149 To represent the exchange of the horizontal momentum due to  
150 the sub-grid scale (SGS) processes, the Laplacian friction form with  
151 Smagorinsky Scheme (Smagorinsky, 1993) was employed. For the  
152 tracer diffusion on the isoneutral surface, the RM scheme for the eddy  
153 induced advective and diffusive flux of tracer (Roberts and Marshall,  
154 1998) was employed. The KPP (K-profile parameterization) boundary  
155 layer mixing scheme (Troen and Mahrt, 1986; Large et al., 1994)  
156 parameterizes the ocean boundary layer depth, vertical diffusivity and  
157 viscosity, and non-local transport in the ESROM.

158 While the longitudinal resolution of the ESROM is varying from  
159 0.06° (about 5 km) near the western boundary to 0.1° (about 10 km)  
160 to the east of 130°E, the latitudinal resolution is fixed to 0.1°. The  
161 horizontal resolution near the western boundary is smaller than or  
162 comparable to the baroclinic Rossby radius of deformation. The  
163 ESROM is, therefore, expected to reproduce the separation of the  
164 EKWC and seasonal variation of the NKCC off the western boundary.  
165 The numbers of the longitudinal and latitudinal grids are 153 and  
166 192, respectively. To resolve the bottom geometry more accurately,  
167 the partial bottom cell scheme was used (Pacanowski and Gnanade-  
168 sikan, 1998) and high resolution bathymetry of 1/60° (Choi et al.,  
169 2002) was adopted for the model topography. The vertical resolution  
170 is varying from 2.64 m at the surface to 445.97 m at the bottom  
171 with 42 vertical levels. There are 14 levels from top to 100 m for the  
172 upper ocean, 9 levels from 100 m to 300 m for the intermediate water,  
173 and 19 levels from 300 m to the bottom of 4000 m. The ESROM has  
174 been integrated asynchronously to reduce the computational cost;  
175 the tracer time step is 2,400 sec, larger than 800 s of the time step  
176 for the momentum equations. The momentum equation has been  
177 also split into the barotropic and baroclinic modes. The model was  
178 initialized using hydrographic data from WOA (World Ocean Atlas,  
179 2002), and forced by monthly mean surface and open boundary  
180 conditions.

### 181 2.1. Surface boundary conditions

182 Surface windstress, heat flux and salt flux are given for the surface  
183 boundary conditions. Monthly mean winds in the EJS have been  
184 computed by Na et al. (1992) and Na and Seo (1998) using weather  
185 charts with a spatial resolution of a few hundred kilometers. Recently,

wind data from the satellite scatterometer with higher resolution of  
25 km reveals the strong northerly wind in winter off the Vladivostok  
due to the orographic effect. Kawamura and Wu (1998) suggested that  
the strong wind causes the large turbulent heat flux and evaporation,  
which generates the dense water mass. The European Centre for  
Medium-Range Weather Forecast (ECMWF) data relatively well  
describes the orographic effect among the reanalyzed products  
(Nam et al., 2005). In particular, the ECMWF resolves the dipole  
structure of the wind stress curl off the Vladivostok and the positive  
windstress curl off the Wonsan Bay (Fig. 1). In this paper, we used the  
reanalyzed wind stress of the ECMWF.

Surface net heat flux ( $Q_{net}$ ) is the sum of downward shortwave  
radiation ( $Q_{sw}$ ), backward longwave radiation ( $Q_w$ ), sensible heat flux  
( $Q_{sen}$ ), and latent heat flux ( $Q_{lat}$ ). All components except shortwave  
radiation are calculated by bulk air-sea flux formulation (Large et al.,  
1997) as

$$Q_{net} = Q_{sw} - (Q_{sen} + Q_{lat} + Q_{lw}) \quad (1)$$

$$Q_{sen} = \rho_a C_p^a C_H W_{10} (T_a - \theta_1) \quad (2)$$

$$Q_{lat} = \rho_a L_e C_E W_{10} (q_a - q_1) \quad (3)$$

$$Q_{lw} = -\varepsilon \sigma_{SB} \left\{ T_a^4 [0.39 - 0.05(e_a)^{0.5}] F(C) + 4T_a^3 (\theta_1 - T_a) \right\} \quad (4)$$

$\rho_a$ ,  $C_p^a$  and  $C_H$  are the air density, specific heat of air, and heat transfer  
coefficient, respectively.  $W_{10}$  and  $T_a$  are wind speed at 10 m height and  
air temperature at 2 m height taken from the meteorological dataset,  
 $\theta_1$  is the sea surface temperature from the ocean model.  $L_e$  and  
 $C_E$  are the latent heat of vaporization and transfer coefficient for  
evaporation, and  $q_a$  and  $q_1$  are the specific humidity and implied  
saturated specific humidity estimated from  $\theta_1$ .  $e_a$  is the surface water  
vapor pressure found from the  $q_a$ , and  $\varepsilon$  and  $\sigma_{SB}$  are the surface  
emissivity and Stefan-Boltzmann coefficient, respectively.  $F(C)$  is the  
cloud fraction factor (Budyko, 1974; Large et al., 1998).

Meteorological variables of  $T_a$ ,  $W_{10}$ ,  $C$  (fraction of the cloud cover),  
and  $q_a$  are listed in Table 1.

For the salt flux, the surface salinity ( $S_{surf}$ ) in the model is relaxed  
to that ( $S_{obs}$ ) of the WOA by

$$S_{surf}^{m+1} = \gamma (S_{obs} - S_{surf}^m) \quad (5)$$

where  $\gamma$  is the reciprocal of the relaxation time scale, which is 10 days,  
and superscript denotes the  $m$ -th time step.

### 2.2. Open boundary conditions

A radiation condition with a nudging term for inward boundary  
fluxes is applied for the tracers and barotropic currents (Marchesiello

**Table 1**  
Meteorological variables for the surface boundary conditions.

Variable	Source	Horizontal Resolution	Time interval	
$\tau_x$	Zonal wind stress	ECMWF	0.5° × 0.5°	12 h
$\tau_y$	Meridional wind stress	ECMWF	0.5° × 0.5°	12 h
$Q_{sw}$	Surface solar radiation downward	ERA40 <sup>a</sup>	1.125° × 1.125°	6 h
$q_a$	Specific humidity	ERA40 <sup>a</sup>	1.125° × 1.125°	6 h
$W_{10}$	10 m wind speed	QuikSCAT	0.25° × 0.25°	12 h
$T_a$	2 m air temperature	ECMWF	0.5° × 0.5°	12 h
$C$	Fraction of the cloud cover	AMIP-II <sup>b</sup>	0.869° × 0.869°	6 h

<sup>a</sup> ECMWF 40 year re-analysis data archive.

<sup>b</sup> NCEP-DOE reanalysis 2.

et al., 2001). The radiation condition for the prognostic variables ( $\phi$ ) is given by

$$\frac{\partial \phi}{\partial t} + C_x \frac{\partial \phi}{\partial x} + C_y \frac{\partial \phi}{\partial y} = -\frac{1}{\tau} (\phi - \phi^{ext}) \quad (6)$$

where  $x$  and  $y$  are the normal and tangential directions to the boundary, and  $t$  is the time.  $\phi^{ext}$  represents the external data and  $\tau$  is the time scale for nudging.  $C_x$  and  $C_y$  are phase speed of the oblique radiations calculated from the  $\phi$  field neighboring the boundary point, which is given by

$$C_x = -\frac{\partial \phi}{\partial t} \frac{\partial \phi / \partial x}{(\partial \phi / \partial x)^2 + (\partial \phi / \partial y)^2} \quad (7)$$

and

$$C_y = -\frac{\partial \phi}{\partial t} \frac{\partial \phi / \partial y}{(\partial \phi / \partial x)^2 + (\partial \phi / \partial y)^2}. \quad (8)$$

The nudging time scale  $\tau$  is give by

$$\tau = \tau_{out} \text{ if } C_x > 0 \quad (9)$$

for inward propagation. And,

$$\tau = \tau_{in} \text{ and } C_x = C_y = 0 \text{ if } C_x < 0 \quad (10)$$

for outward propagation with  $\tau_{out} \gg \tau_{in}$ .

In addition, it is assumed that there is no gradient of the sea surface elevation across the boundaries following Marchesiello et al. (2001).

For the mass (volume) conservation, a correction velocity is added to the barotropic velocity obtained from the radiation condition by

$$\bar{u}_{new} = \bar{u} - \bar{u}_c \vec{n} \quad (11)$$

where  $\bar{u}$  is the barotropic velocity,  $\bar{u}_c$  is a normal velocity correction and  $\vec{n}$  is the unit inward vector at the open boundaries.  $\bar{u}_c$  is given by

$$\bar{u}_c = \frac{1}{S_b} \left( \int_{L_b} h \bar{u} \cdot \vec{n} dL - F \right) \quad (12)$$

where  $S_b$  and  $L_b$  are the total surface area and total perimeter of the open boundaries, and  $h$  is the depth.  $F$  means the volume change over the whole domain due to the sinks or sources and  $F=0$  in this paper.

The ESROM has three open boundaries. The barotropic velocity through the Korea Strait is given by the volume transport monitored by the submarine cable (Kim et al., 2004). The same amount of the inflowing water volume flows out through the Tsugaru Strait and Soya Strait, and the volume transport through the Tsugaru Strait is given twice the transport through the Soya Strait (Na et al., 2007–this issue).

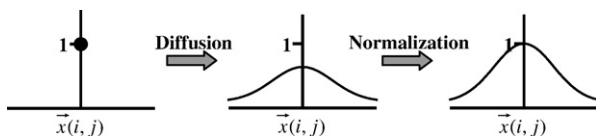


Fig. 2. Schematic diagram for the normalization factor  $\Lambda$ .

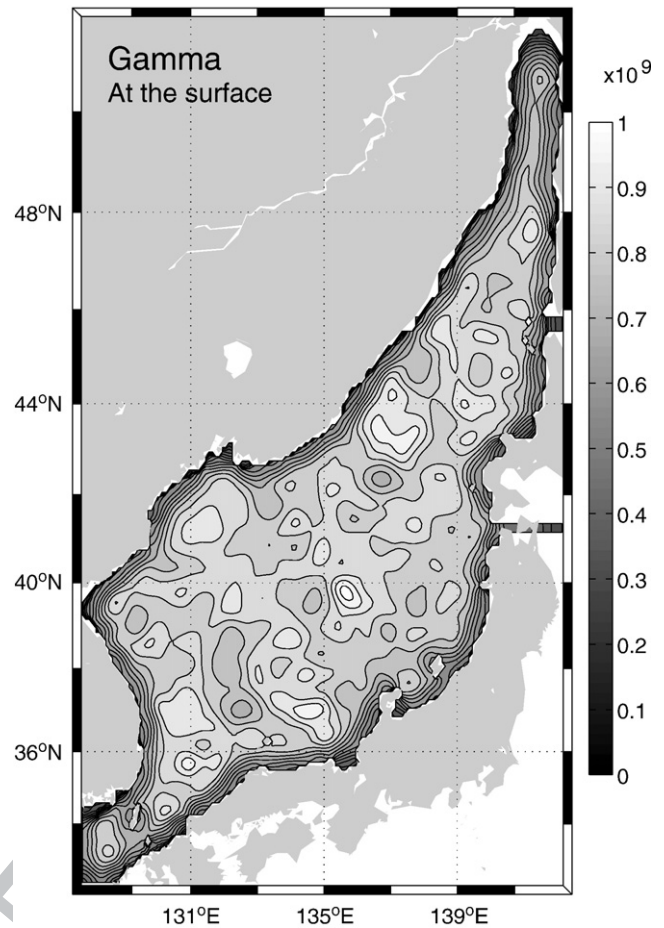


Fig. 3. Normalization factor  $\Lambda$  at the surface for the DA-ESROM estimated by the randomization method.

The temperature and salinity of the inflow are relaxed to the WOA hydrographic dataset with a 5 day-timescale.

### 3. 3-Dimensional variational assimilation technique

Weaver and Courtier (2001) proposed the use of the diffusion equation to construct 2-dimensional and 3-dimensional univariate correlation models. In this paper, the basic formulation and terminology for the 3-dimensional variational technique follow Weaver and Courtier (2001) since these correlation models are numerically efficient and support the various shape of correlation functions, for example, complex geography. The 3-dimensional variational assimilation routine has been fully coupled with the ESROM (hereafter, DA-ESROM), and temperature profiles and satellite datasets have been assimilated. The 3-dimensional variational assimilation module formulated in this work has a general form so that it can be applied not only to the EJS but also to other regions.

Following Weaver and Courtier (2001), the background error covariance for the uni-variate variational assimilation can be written as

$$B = \Sigma C \Sigma \quad (13)$$

where  $C$  is a symmetric background error correlation matrix and  $\Sigma$  a diagonal background error standard deviation matrix. By defining a new variable  $v = B_{\Lambda}^{-1/2} \delta x$  following Courtier (1997) and Derber and

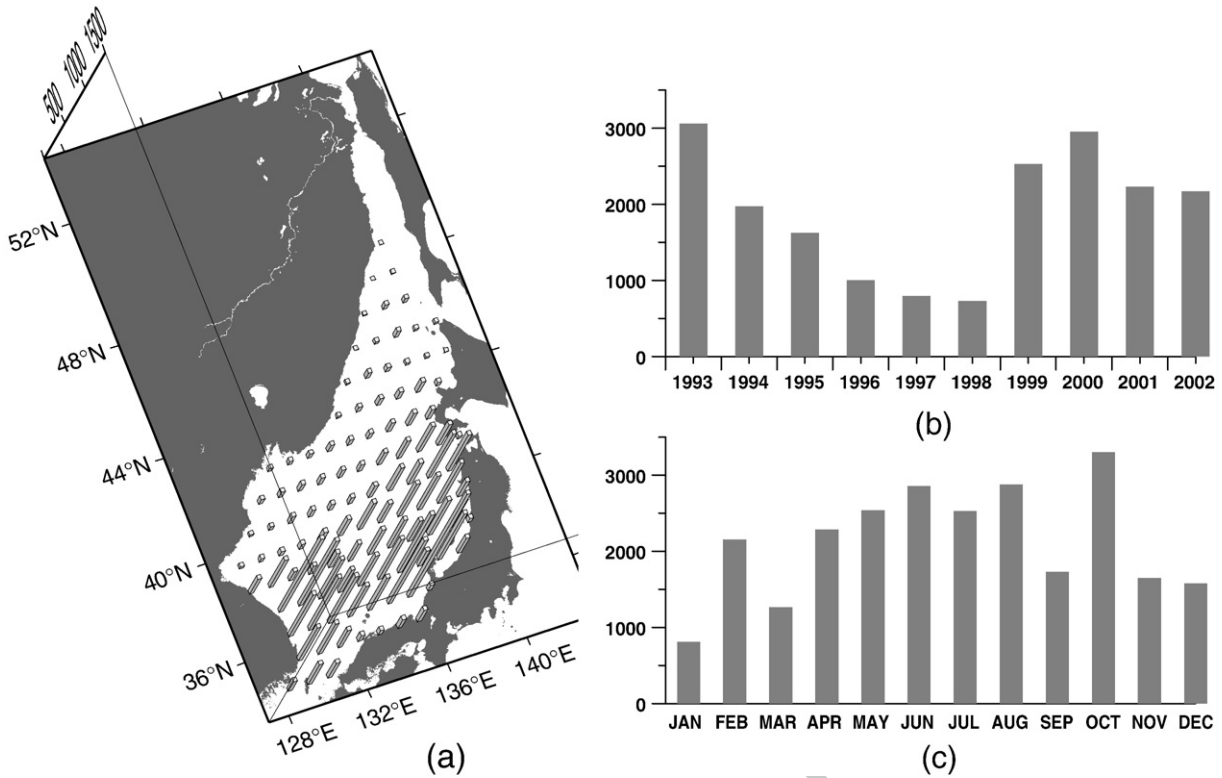


Fig. 4. Amounts of observed temperature profiles from KODC, JODC, CREAMS and Argo floats in horizontal (a), in year (b) and in month (c).

285 **Bouttier (1999)**, the analysis increment and the gradient of the cost  
286 function are given by

$$\delta x^a = \Sigma C^{1/2} v \quad (14)$$

$$\nabla J(v) = v + C^{T/2} \Sigma \nabla_{\delta x} J_o \quad (15)$$

289 where  $\delta x$  is an increment of the background state vectors,  $C^{1/2}$  is  
291 defined from  $C = C^{1/2} C^{1/2}$ , and

$$\nabla_{\delta x} J_o = H^T R^{-1} (H \delta x - d) \quad (16)$$

293 where  $R$  and  $H$  are the assumed observation error covariance matrices  
294 and the observation operator,  $d$  represents the observation state  
295 vectors, and the superscript  $T$  denotes the transpose of the matrix.  $R$  is  
296 a diagonal matrix under assumption of uncorrelated observation  
297 errors, and contains instrumental errors and representativeness  
298 errors. The representativeness error is caused by the misrepresentation  
Q4299 of all scales smaller than observation network scales (Daley,  
300 1991), which is much larger than the instrumental error generally. In  
301 this study, the root-mean-square observation error is 1.0 °C for  
302 temperature profiles, 1.5 °C for SST and 5.0 cm for SSHA.

### 303 3.1. Correlation modeling using the diffusion equation

304 Starting point is the 2-dimensional horizontal diffusion equation  
305 and the solution of a general partial differential equation to the model  
306 variables  $\eta$  can be considered as follows:

$$\frac{\partial \eta}{\partial t} + \sum_{p=1}^P \kappa_p (-\nabla^2)^p \eta = 0 \quad (17)$$

where  $\kappa_p$ ,  $p = 1, \dots, P$ , are non-negative diffusion coefficients. Follow-  
ing the classical solution of the diffusion equation with  $K_p = 0$  for all  
309  $p > 1$ , Eq. (17) can be rewritten as  
310

$$\frac{\partial \eta}{\partial t} - \kappa_h (\nabla^2) \eta = 0 \quad (18)$$

where  $\kappa_h$  is the horizontal diffusion coefficient. The solution of  
312 Eq. (18) can be represented by using the discrete diffusion operator  $D_h$   
313 in 2-dimension as  
314

$$\eta(t_M) = L_h \eta(t_0) \quad (19)$$

where  $t_M$  is the time at  $M$  steps after the initial time  $t_0$ , and  $L_h$  is given  
316 by  
317

$$L_h = \{I + \kappa_h \Delta t D_h\}^M \quad (20)$$

where  $D_h$  denotes a matrix representing the discretized Laplacian.  $D_h$   
318 is self-adjoint and may satisfy  $D_h = W_h^{-1} D_h^T W_h$  where  $W_h$  is a diagonal  
320 matrix of local area element. From Eq. (20),  $L_h$  can be factored as  
321

$$\begin{aligned} L_h &= L_h^{1/2} L_h^{1/2} \\ &= \{I + \kappa_h \Delta t D_h\}^{M/2} \{I + \kappa_h \Delta t D_h\}^{M/2} \\ &= \{I + \kappa_h \Delta t (W_h^{-1} D_h^T W_h)\}^{M/2} \{I + \kappa_h \Delta t D_h\}^{M/2} \\ &= W_h^{-1} \{I + \kappa_h \Delta t (D_h^T)\}^{M/2} W_h \{I + \kappa_h \Delta t D_h\}^{M/2} \\ &= W_h^{-1} L_h^{T/2} W_h L_h^{1/2} \\ &= L_h^{1/2} W_h^{-1} L_h^{T/2} W_h \end{aligned} \quad (21)$$

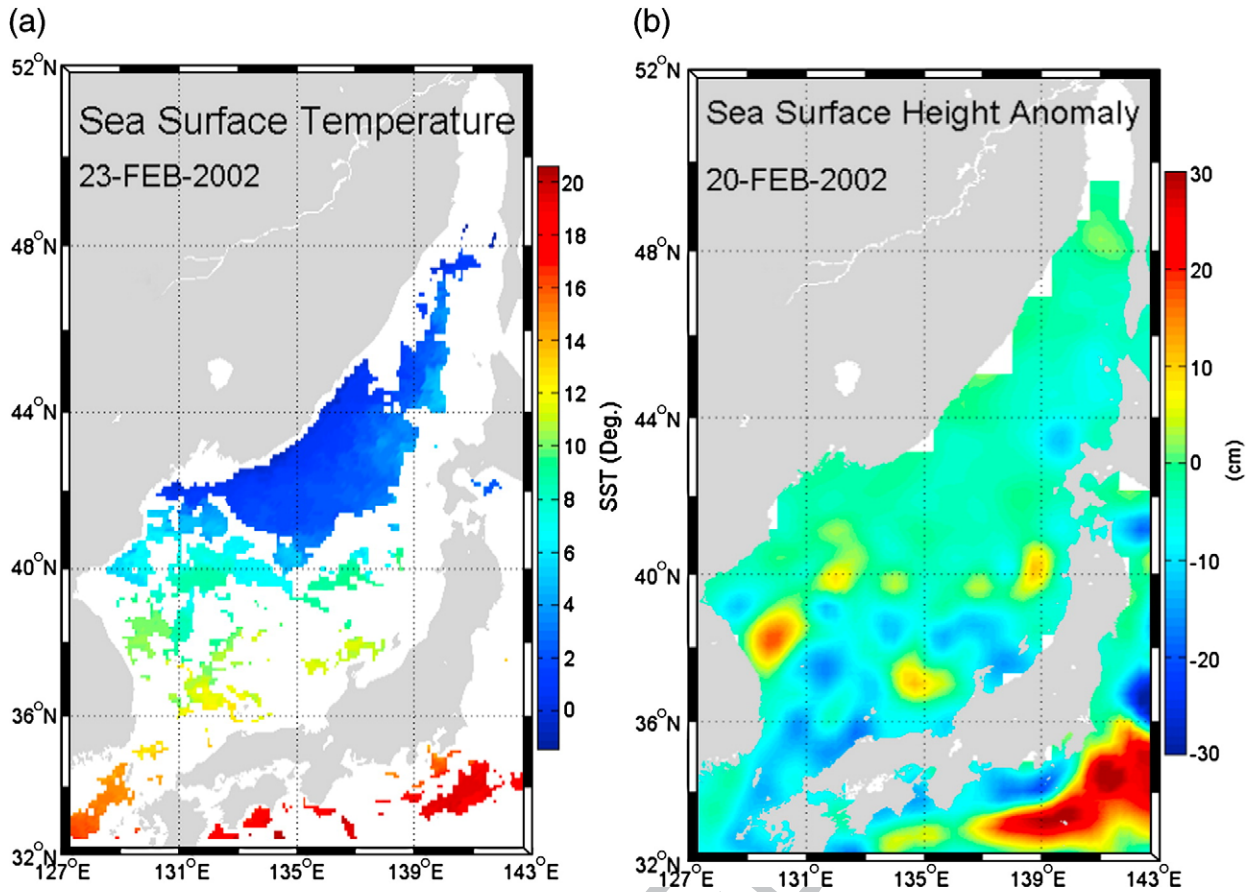


Fig. 5. Examples of SST (a) and DT-MSLA (b) in February, 2002.

324 A normalization matrix  $\Lambda$  is introduced to convert Eq. (21) into a  
 325 correlation matrix: i.e.  $\Lambda$  ensures that the auto-correlation is identity.  
 326 Then, the correlation matrix can be given by

$$\begin{aligned} C &= \Lambda L_h^{1/2} W_h^{-1} L_h^{T/2} \Lambda \\ &= \left( \Lambda L_h^{1/2} W_h^{-1/2} \right) \left( \Lambda L_h^{1/2} W_h^{-1/2} \right)^T \\ &= C^{1/2} C^{T/2}. \end{aligned} \quad (22)$$

328 In a multi-level ocean model, the error correlation model is  
 329 required in the vertical as well as in the horizontal. Fundamentally, the  
 330 error correlation model in the vertical has the same form as before but  
 331 in the 1-dimension. The Laplacian diffusion operator in the vertical  
 332 can thus be represented as

$$L_v = \{I + \kappa_v \Delta t D_v\}^M. \quad (23)$$

333 Now, we can express the 3-dimensional covariance operator as

$$\begin{aligned} L_v W_v^{-1} L_h W_h^{-1} &= L_v^{1/2} W_v^{-1} L_v^{T/2} L_h^{1/2} W_h^{-1} L_h^{T/2} \\ &= L^{1/2} W^{-1} L^{T/2} \end{aligned} \quad (24)$$

338 where  $W = W_h W_v$  and  $L = L_v L_h$ . Finally, the square-root form of the  
 339 3-dimensional correlation matrix for Eqs. (15) <sub>$\Lambda$</sub> –(16) can be given by

$$C^{1/2} = \Lambda L^{1/2} W^{-1/2} \quad (25)$$

$$C^{T/2} = W^{-1/2} L^{T/2} \Lambda. \quad (26)$$

In this 3-dimensional correlation matrix, the ‘adjoint’ operator  $D_h^{T/2}$  344  
 and  $D_h^{1/2}$ , corresponding to  $D_h^{1/2}$  and  $D_v^{1/2}$  respectively, are required. 345

At the end, the normalization factor  $\Lambda$  is required to construct 346  
 the correlation matrix from the diffusion model as discussed 347  
 previously. As shown in Fig. 2, the  $\Lambda$  ensures that the auto-correlation 348  
 is identity. 349

The exact estimation of  $\Lambda$  is given by the diagonal elements of the 350  
 matrix  $LW^{-1}$ , i.e.  $t_l = e_l^T L W^{-1} e_l$  with  $1/\sqrt{t_l}$  defining the  $l$ -th diagonal 351  
 element of  $\Lambda$  where  $e_l = (0, \dots, 0, 1, 0, \dots, 0)^T$ . However, since it is too 352  
 expensive to calculate the exact estimation of  $\Lambda$ , a randomization method 353  
 was proposed as an economic alternative (Fisher and Courtier, 1995; 354  
 Andersson et al., 2000). Considering the transformation  $v' = L^{1/2} W^{-1/2} v$  355  
 where  $v$  is a Gaussian random variable having zero mean and unit 356  
 variance, the diagonal elements of the matrix  $LW^{-1}$  can be estimated by 357

$$LW^{-1} \approx \frac{1}{Q} \sum_{q=1}^Q v_q v_q^T = \frac{1}{Q} \sum_{q=1}^Q \left( L^{1/2} W^{-1/2} v_q \right) \left( L^{1/2} W^{-1/2} v_q \right)^T \quad (27)$$

where  $Q$  is the number of random vectors equal to 200 in this work. 358  
 The estimated  $\Lambda$  by the randomization method at the surface is 360  
 displayed in Fig. 3. 361

### 3.2. Assimilation of satellite altimeter data 362

Satellite altimeter data are now considered to be the most 363  
 important input for the ocean data assimilation since they can cover 364  
 wide spatial range during relatively short period. Among several 365  
 different methods to assimilate the sea surface height (SSH) into 366  
 ocean models, we followed Cooper and Haines (1996). Their method 367  
 is to rearrange preexisting water masses under an assumption of 368

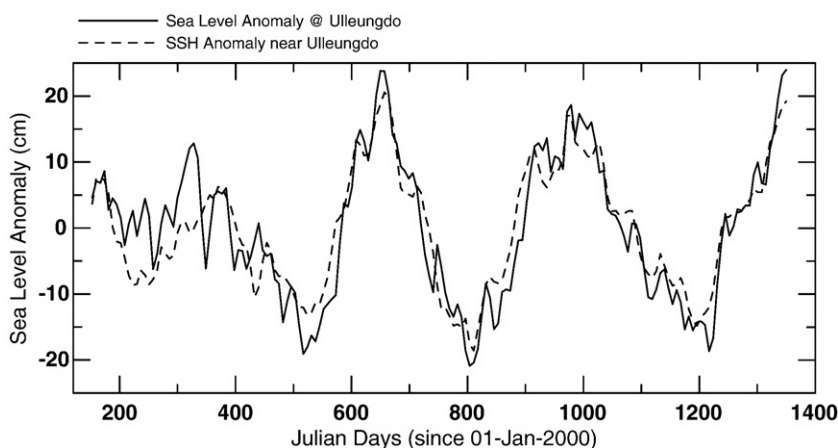


Fig. 6. Comparison between observed sea level anomaly from the tidal station and merged multi-satellite SSHA.

369 conservation of water properties and potential vorticity. The simple  
 370 way of Cooper and Haines (1996) to satisfy the conservation  
 371 assumptions is to displace water columns so that the change in the  
 372 surface pressure should be compensated by the change in weight of  
 373 the entire water columns, which will ensure the bottom pressure are  
 374 not altered. This constraint gives the following relationship

$$g \int_0^{-H} \Delta \rho dz = \Delta p_s \quad (28)$$

376 where  $\Delta \rho$  and  $\Delta p_s$  are the changes in density of the water columns and  
 377 surface pressure from the satellite altimeter. If the low surface  
 378 pressure ( $\Delta p_s < 0$ ) is observed, the water column should be lifted up

by some displacement  $\Delta h$  with adding heavy water at the bottom and  
 removing light water at the surface as following 380

$$\begin{aligned} \Delta p_s + g\rho(0)\Delta h - \int_{-H+\Delta h}^{-H} g\rho(z)dz &= 0, \text{ if } \Delta p_s > 0 \\ \Delta p_s - \int_0^{\Delta h} g\rho(z)dz + g\rho(-H)\Delta h &= 0, \text{ if } \Delta p_s < 0 \end{aligned} \quad (29)$$

If the variation of density near the bottom and the surface are  
 negligible, from Eq. (29),  $\Delta h$  is given by 384

$$\Delta h = \frac{\Delta p_s}{g[\rho(0) - \rho(-H)]} \quad (30)$$

$\Delta h$ , in practice, is calculated through iteration of Eq. (30) instead of  
 Eq. (29) until Eq. (28) is satisfied. Before the displacement of the 388

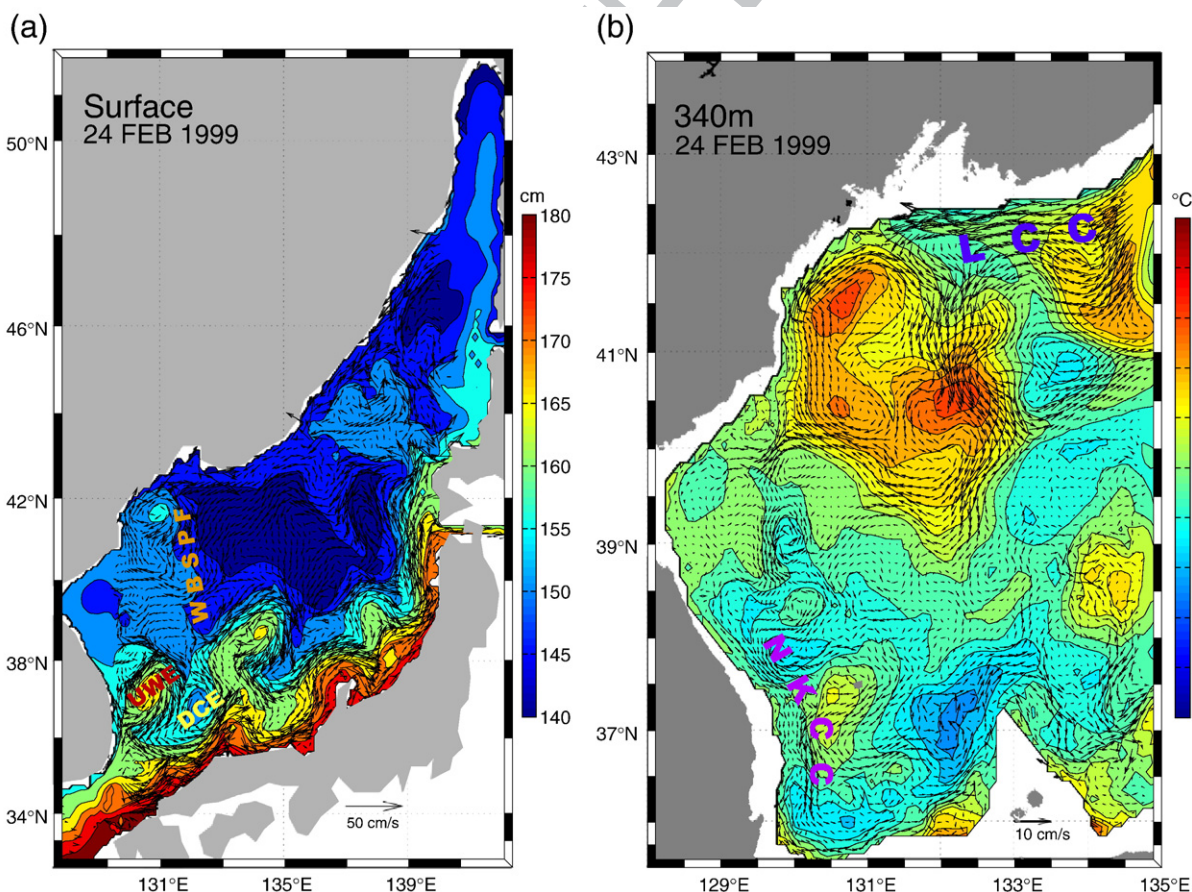


Fig. 7. Sea surface height and current (a), and temperature and current at 340 m (b) produced by the DA-ESROM on 24 February 1999.

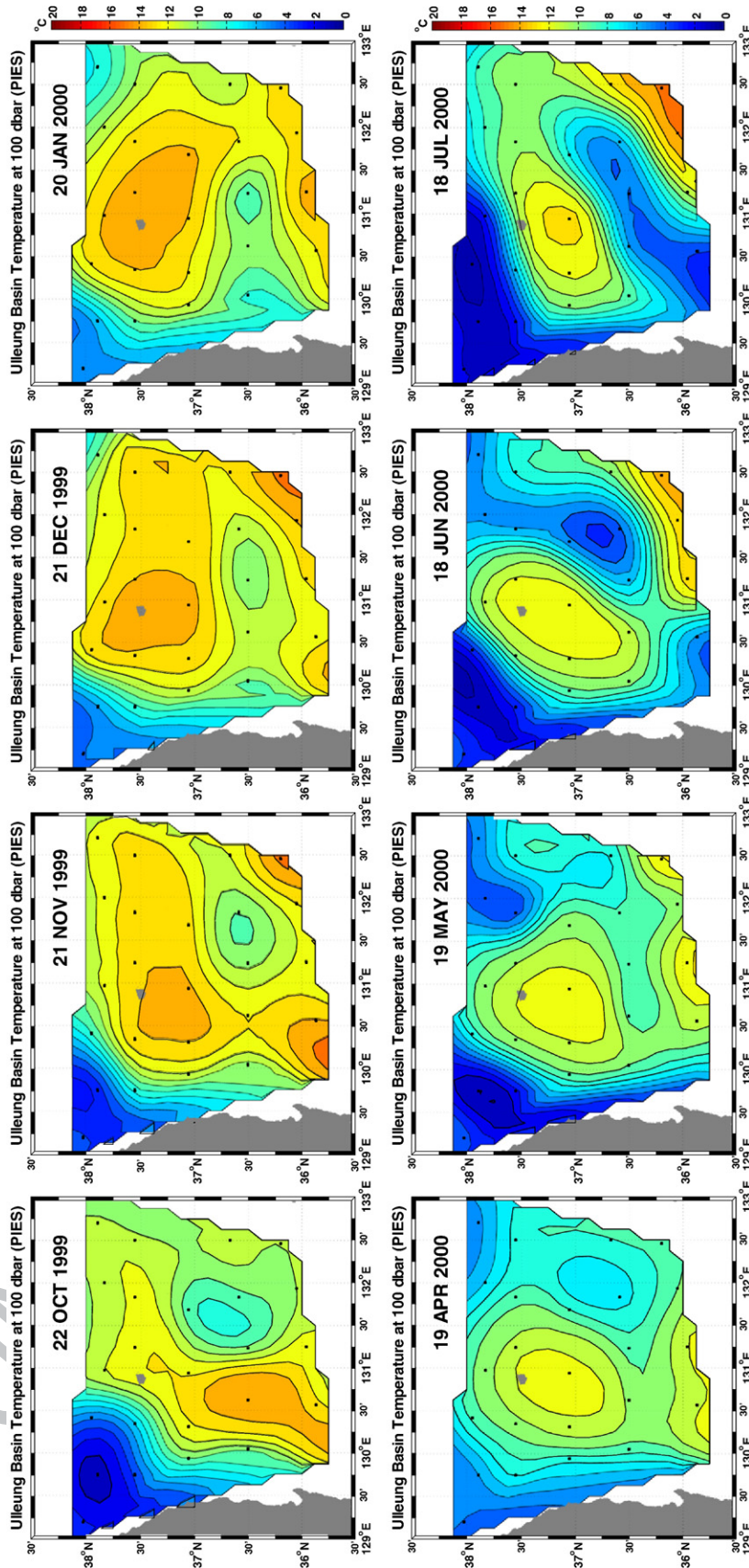


Fig. 8. Snapshots of 100-dbar temperature fields from PIES data between October, 1999 and July 2000. Mitchell et al. (2005a).



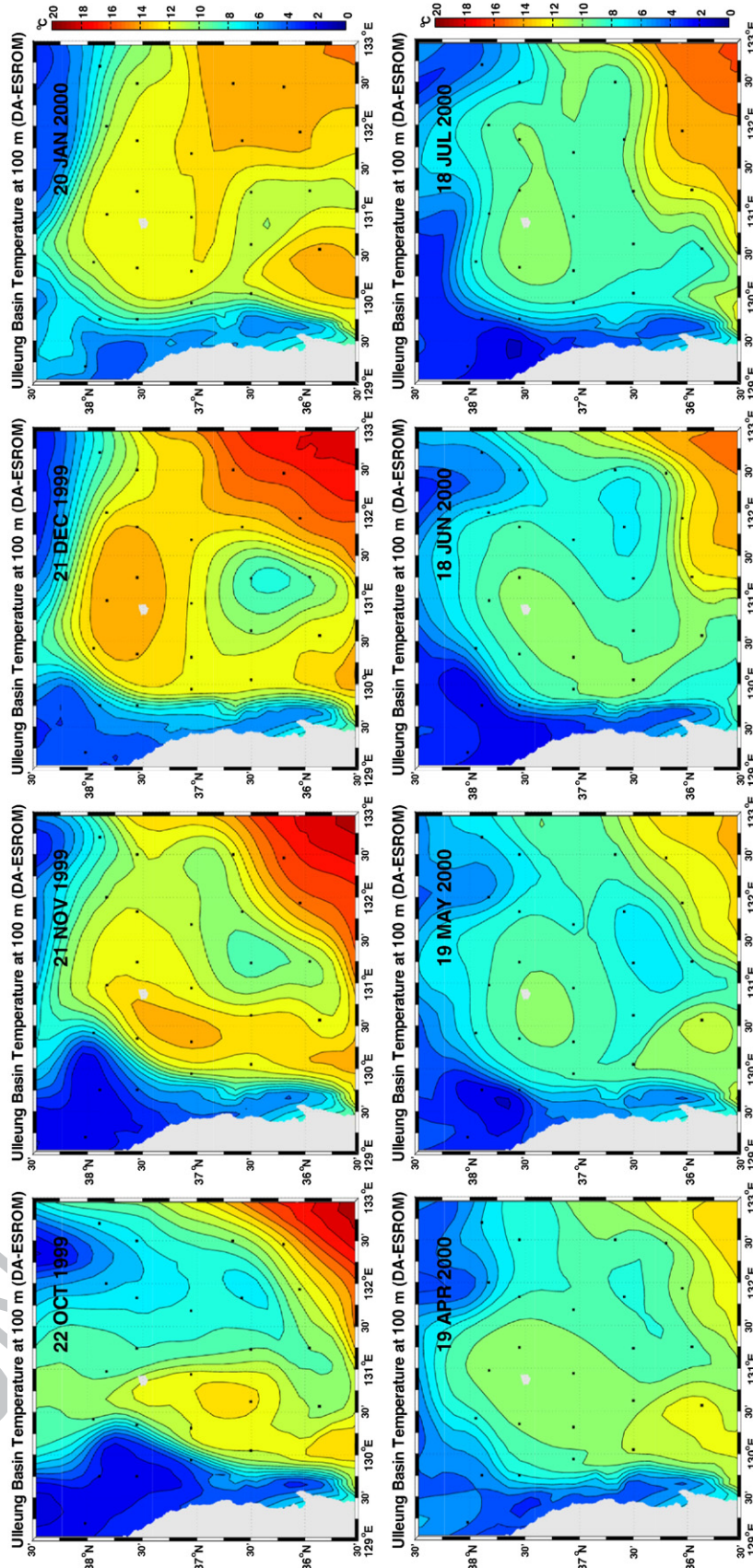


Fig. 9. Snapshots of 100 m temperature fields produced by the DA-ESROM at the same dates in Fig. 8.

water columns, a spline fitting is applied to the preexisting water columns for a better representation of the water properties. After the displacement of the water columns, current may be adjusted geostrophically.

The satellite SSH data are available at the observation grid points while the sea surface pressure is required at all horizontal grid points. Hence, two dimensional mapping of the satellite altimeter data is performed prior to applying the 3-dimensional assimilation routine.

Additionally, the geoid error cannot be negligible in the marginal seas. In this paper, the SSH increment from SSH of the previous step is assimilated into the model instead of the SSH itself as following

$$\eta_k^a = \eta_k^f + K[(y_k - y_{k-1}) - H(\eta_k^f - \eta_{k-1}^a)] \quad (31)$$

where  $\eta_k^a$  and  $\eta_k^f$  are SSH analysis and forecast fields in the  $k$ -th assimilation step, and  $K$  is the Kalman gain matrix. Therefore, observed SSH  $y_k$  can be replaced with SSHA.

### 3.3. Preparation of observation datasets for the DA-ESROM

CTD profiles, satellite datasets of SST and SSHA were assimilated into the ESROM. The distribution of temperature profiles assimilated into the model is shown in Fig. 4. High-density temperature profiles in the southern region (Fig. 4a) are mainly archived from KODC (Korea Oceanographic Data Center) and JODC (Japan Oceanographic Data Center). Temperature profile data are scarce in the northern region, where the main data sources are CREAMS (Circulation Research of the East-Asian Marginal Seas) Expedition and Argo datasets. Since the data quality of the salinity from the CTD profiles is not fully credible, only temperature data are used.

The number of temperature profiles varies from year to year in Fig. 4b. The large number in 1993 mainly comes from CREAMS data and Japanese observation programs. Though the CREAMS Expedition has conducted hydrographic surveys just once or twice a year it provides useful data for the data assimilation because the coverage of the CREAMS surveys includes the northern region of the EJS where the profile data are insufficient. The number of profiles decreased from 1993 to 1998, and increased sharply in 1999 after the deployment of Argos as a part of the U.S. EJS program.

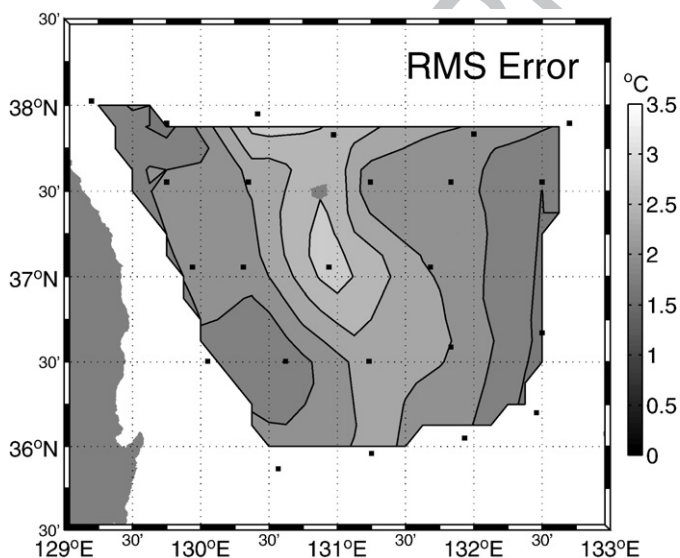


Fig. 10. Root mean square (RMS) error between 100 m/100-dbar temperature fields by the DA-ESROM and from the PIES measurements.

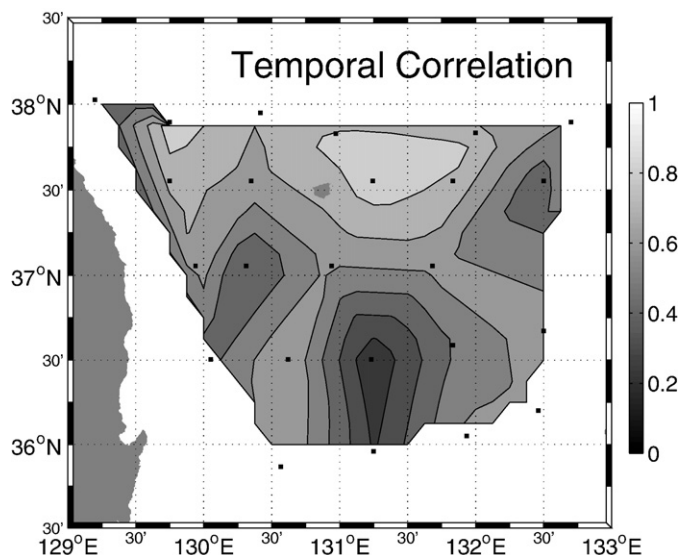


Fig. 11. Temporal correlation between 100 m/100-dbar temperature fields from the DA-ESROM and PIES measurements.

The number of profiles is larger in even months than in odd months because the serial hydrographic datasets from KODC have been obtained in every even month (Fig. 4c). The number of profiles increases in summer and decreases in winter, which appears to be due to the seasonal difference in sea states. A number of Argo floats deployed since 1999 provides useful data, especially in the northern EJS (Fig. 4b).

All temperature profiles are assimilated at mid of each month after data quality control procedure. The quality control procedure includes the correctness of time and position, de-spiking, and removal of temperature inversions and outliers as compared with global ranges. In addition, single valued or duplicate profiles are excluded.

The NODC/RSMAS AVHRR Oceans Pathfinder SST Version 5.0 data are sub-sampled every 16 km and then assimilated into the surface level of the ESROM every day. As shown in Fig. 5a, most SST images could not cover the whole area of the EJS due to cloud covers. Nevertheless, they have a good coverage in the northern region of the EJS where the ship measurement is difficult, and the assimilation of SST data is thought to be necessary for reproducing the convective condition in the ESROM.

The merged SSHA of the DT-MSLA (Delayed Time-Merged Sea Level Anomaly) produced by the AVISO has been assimilated into the ESROM every 7 days. The DT-MSLA provided by the AVISO is a merged product which combines TOPEX/POSEIDON, Jason-1, ERS-1/2, ENVISAT, and GFO data. High frequency (2–20 days) sea level fluctuations, driven by atmospheric pressure changes, can induce an aliasing problem to altimeter data sampled at satellite orbit frequency since it is difficult to correct the nonisostatic sea level response with the standard inverse barometer (IB) method. When the IB method is applied to correct the nonisostatic sea level response, the aliasing signal can reach 10 cm (Nam et al., 2004). Nam et al. (2005), however, showed that the aliasing signal is significantly reduced through the process of merging with multiple-satellite altimetry data. The merged multiple-satellite altimetry data, in fact, are comparable with the sea level data observed at Ulleungdo (Fig. 6).

### 4. Comparison between reanalyzed products and observations

Continuous acoustic travel-time was measured from a two-dimensional array of pressure-gauge-equipped inverted echo sounders (PIES) in the UB during 2 years between June 1999 and July 2001.

A three-dimensional time-series of synoptic current and temperature fields with an accuracy of 1.5 °C was obtained using the residual gravest empirical mode (Residual GEM) technique (Mitchell et al., 2005a). From the daily temperature fields for 2 years, Mitchell et al. (2005a,b) identified five flow patterns in the UB, and showed, for the first time, the presence of the highly variable Dok Cold Eddy (DCE) in the UB. They used temperature fields the 100-dbar lying below the surface layer and within the main thermocline. We compared the 100-dbar temperature fields from PIES data and 100 m temperature fields produced by the DA-ESROM to validate the performance of the DA-ESROM. We also analyzed model-produced NKCC flowing southward under the EKWC, the seasonal variation of which has not been properly simulated in the previous EJS modeling studies (Kim and Yoon, 1999; Yoshikawa et al., 1999; Lee et al., 2003).

#### 4.1. High variability of the EKWC, Ulleung Warm Eddy (UWE) and DCE in the UB

The DA-ESROM has reproduced the well-known general features of the circulation in the EJS. According to the model result in February 1999, the TWC splits into three currents, the EKWC flowing northward along the east coast of Korea, Nearshore Branch (NB) off the Japanese coast, and the Offshore Branch in between them. The separation latitude of the EKWC from the Korean coast is at the south of 37°N. The Liman (or Primoriye) Cold Current (LCC) flows southward along the Primoriye coast and separates from the coast along the Western Branch of the Subpolar Front (WBSPF) which has been recently reported by Park et al. (2004). The NKCC underlying the EKWC flows southward along the eastern coast of Korean. The DA-ESROM has also well represented the mesoscale variability in the UB such as the UWE (Chang et al., 2004) and the DCE (Fig. 7).

Comparing model results with those from Mitchell et al. (2005a) (Fig. 8), the DA-ESROM fairly well simulates the high variability of the UWE and DCE in the UB (Fig. 9). From October, 1999 until January, 2000, the UWE moved northward while its zonal size was almost doubled. Simultaneously, the DCE propagated westward and collapsed when it collided with the east coast of Korea. The variability of the UWE is relatively weak from April to July, 2000, when it resided around the Ulleungdo and its size was rarely changed. The DCE, however, experienced a series of its evolution from its formation, westward propagation, and to the collapse near the coast of Korea. The UWE and DCE also had an influence on the EKWC. The separation position of the EKWC moved northward as the UWE did. Sometimes, the DCE interrupted the northward flow of the EKWC; as the DCE approached

the east coast of Korea, the EKWC separated further south in January, 2000 or even it disappeared along the Korean coast in July, 2000.

Fig. 10 shows the root-mean-square (RMS) error ( $\varepsilon$ ) between the 100 m/100-dbar temperature fields by the DA-ESROM and from the PIES measurement, which is given by

$$\varepsilon = \sqrt{(T_{DA} - T_{PIES})^2} \quad (32)$$

where  $T_{DA}$  and  $T_{PIES}$  are 100 m/100-dbar temperature fields by the DA-ESROM and PIES measurement respectively and overbar ( $\bar{\quad}$ ) denotes the temporal mean from June, 1999 to July, 2001. The overall RMS difference is 2.1 °C. The temperature fields of the DA-ESROM appear to be reasonable when the accuracy of the Residual GEM Technique is 1.5 °C. The RMS error is relatively low with values less than 2.0 °C in the outside of the UB while it is high with values ranging from 2.5 to 3.0 °C around the center of the UB and the north of the Ulleungdo.

Fig. 11 shows the temporal correlation between 100 m/100-dbar temperature fields of the DA-ESROM and PIES measurements, which has quite different spatial feature from that of the RMS error. It is found that there is a high temporal correlation over 0.7 at the north of 37°N. It is interesting to note that the spatial correlation is high around Ulleungdo where the RMS error is high. The high RMS error and temporal correlation between the DA-ESROM and PIES measurements imply the high variability of the EKWC and UWE at that region. Low correlation less than 0.3 is found in the middle of southern UB where the observed data, assimilated into the DA-ESROM, were scarce.

While the spatial correlation between temperature fields by DA-ESROM and from PIES measurements is high with a mean value of 0.79, the spatial correlation is low in February, 2000 and June, 2001 etc. (Fig. 12), when the DA-ESROM could not well resolve the UWE in terms of its position and size (not shown here).

#### 4.2. North Korean Cold Current/Water

The DA-ESROM reproduces the seasonality of the NKCC qualitatively coinciding with observational results. Model results show that the southward NKCC, originating from the Japan Basin, strengthened along the Korean coast from April until August in 1999 with a maximum speed of about 10 cm/s and its width of about 35 km from the coast (Fig. 13). The southward NKCC along the east coast of Korea turned cyclonically around the Japanese coast at the southernmost edge of the UB. The southward currents along the Korean coast weakened in October, and northward currents appeared north of 38°N.

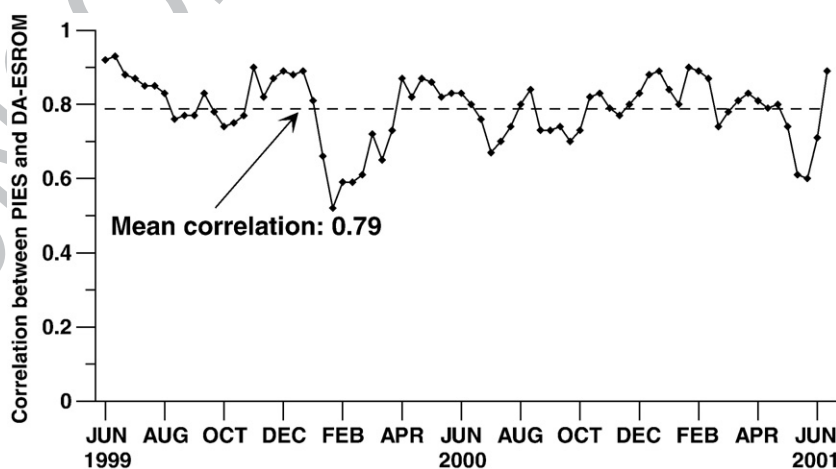


Fig. 12. Spatial correlation between 100-dbar temperature fields from the DA-ESROM and PIES measurements. The mean correlation is 0.79.

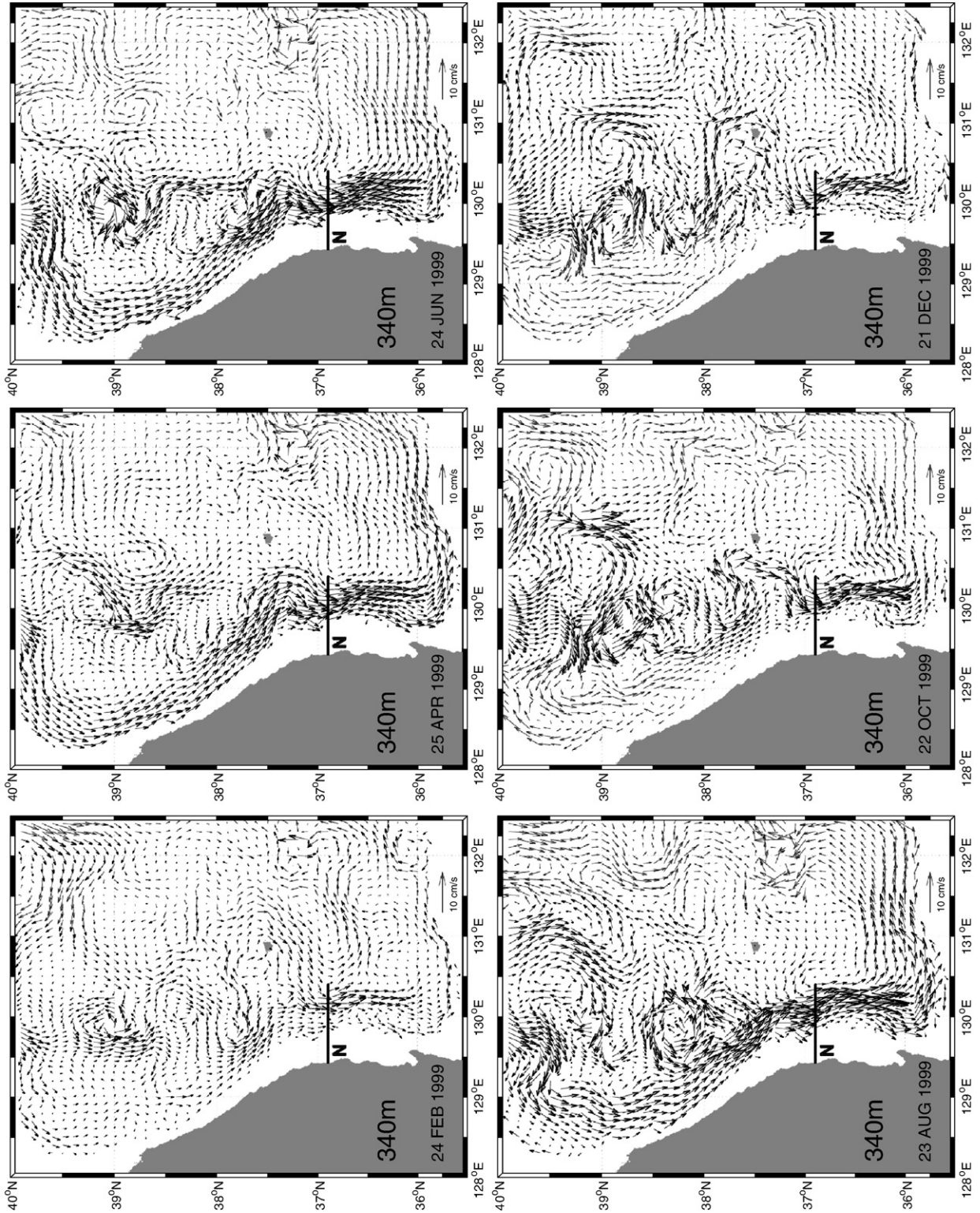
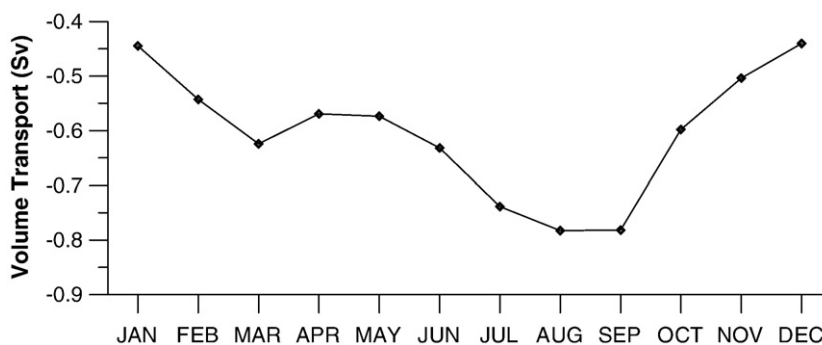


Fig. 13. Currents at 340 m produced by the DA-ESROM in February, April, June, August, October and December 1999.



**Fig. 14.** Monthly mean southward volume transport of the NKCC across line N shown in Fig. 13 during the model simulation period from 1993 to 2002. Volume transport is calculated by integrating southward velocity from 100 m to 700 m. Negative value indicates the southward volume transport.

The volume transport of the NKCC is computed by integrating the southward velocity along the line N from 100 to 700 m. Monthly mean volume transport of the NKCC shows clear seasonality (Fig. 14). The volume transport has the maximum of about 0.8 Sv in August–September and minimum of 0.45 Sv in December–January. In particular, the volume transport is over 0.7 Sv from July to September. Secondary maximum of the monthly mean volume transport occurs in March. During the entire integration period, the model produced the maximum volume transport of 1.6 Sv in August, 1999, which is comparable with the inflow volume transport through the Korea Strait (Kim et al., 2004).

Though the DA-ESROM has successfully reproduced the seasonality of the NKCC, there is a limitation in representing the detail hydrographic and current structure. In vertical sections of temperature, salinity and current in May, 2000, the depth of SML in the DA-ESROM is still deeper by about 50 m as compared to the observation made in the same period (Chang et al., 2002). The speed of the NKCC in the model is also weaker than that in the observation. The SML shifts offshore in the model, while it hugs the Korean coast according to the observation. In addition, the northward surface current seen in the observation east of 130.4°E was not reproduced in the DA-ESROM. These discrepancies of the DA-ESROM may be due to either the poor grid resolution or unresolved geometric feature. Nevertheless, it is notable that the DA-ESROM reproduced shallower SML depth and stronger NKCC as compared with other model results (Fig. 15).

## 5. Conclusion and discussion

Data assimilative numerical model, DA-ESROM, was run in the EJS over the period of 1993 to 2002, and model-data intercomparison was made by comparing the DA-ESROM results with observations. The SST and SSHA from satellites and temperature profiles taken from CREAMS program, KODC, JODC, and ARGO profiling floats have been assimilated into the DA-ESROM.

It is evident that the DA-ESROM reproduced the mesoscale variability as well as the general circulation in the UB even though the comparison is confined for two years from June, 1999 to July 2001. The spatial correlation between the 100 m/100-dbar temperature fields of the reanalyzed products by the DA-ESROM and from the PIES measurements is relatively high with a mean value of 0.79, though it is low in February, 2000 and June, 2001 and the temporal correlation is relatively poor in the middle area of the southern UB. Furthermore, the DA-ESROM has well represented the development and movement of the UWE, and the formation and westward propagation of the DCE. The results of the DA-ESROM suggest that the SSHA may be the influential dataset to represent the mesoscale variability. In this work, the SSHA assimilation technique controls not only the surface features but also the subsurface features every 7 days, which may be enough short to represent high-frequency variability such as the UWE and DCE.

Fig. 16 is a schematic of the circulation pattern in the UB inferred from the reanalyzed products by the DA-ESROM in April, 1999, which shows that the TWC branched into the EKWC, Nearshore Branch and Offshore Branch, and the NKCC, originating from the western Japan Basin, flowed southward along the Korean coast and turns around the Japanese coast at the southernmost edge of the UB. The UWE and DCE also developed in the UB.

The DA-ESROM has successfully reproduced the southward NKCC in summer, and the volume transport of the NKCC in the DA-ESROM suggests that the NKCC strengthens from spring to summer and is strongest in summer. The development of the strong southward NKCC is consistent with the previous observational result (Kim and Kim, 1999). The DA-ESROM shows that the NKCC has the maximum volume transport of about 0.8 Sv in August–September and the minimum volume transport of 0.45 Sv in December–January. The calculated width of the NKCC is about 35 km.

The DA-ESROM contributes to ocean modelling efforts in the EJS in terms of its successful reproduction of the observed NKCC, which has not been so successful in other model studies. In fact, the ESROM without data assimilation module has also reproduced the seasonality of the NKCC, and the main reason for this is thought to be due to the incorporation of the isoneutral mixing scheme and SOM tracer advection scheme. The isoneutral mixing scheme may suppress the Veronis effect to lead spurious diapycnal tracer mixing. In addition, the spurious diapycnal tracer mixing can also be derived numerically through the tracer advection scheme. Hofmann and Maqueda (2006) showed that the SOM scheme much suppresses the numerical diapycnal tracer mixing. High-resolution numerical models like the DA-ESROM are also required to resolve the narrow NKCC. The width of the NKCC is only about 35 km in the DA-ESROM.

For this study, we have employed the MPI (Message Passing Interface) to reduce the computation time for the ocean model and data assimilation routine through the parallel processing. About 20 min elapsed for the forward ocean model and another 20 min for the data assimilation every one month time window using 30 processors of the eServer BladeCenter JS20 (PowerPC 970 2.2 GHz), IBM in Seoul National University, Korea. It is expected that the performance of the DA-ESROM is sufficient enough to be applied to an operational ocean forecast system.

In the 3-dimensional variational technique, the background error covariance is assumed to be the Gaussian form. It is difficult to consider the flow-dependent background error covariance in the 3-dimensional variational technique, despite the fact that the information of the ocean state may follow the ocean flow. Additionally, the SSH assimilation method by Cooper and Haines (1996), employed in this work, could not imply the dynamical processes during the data assimilation. To overcome the limitation, development of an alternative data assimilation system using the Ensemble Kalman Filter (EnKF; Evensen, 1994) is in progress. Though the EnKF requires great computational cost compared to the 3-dimensional variational technique, it is easy to

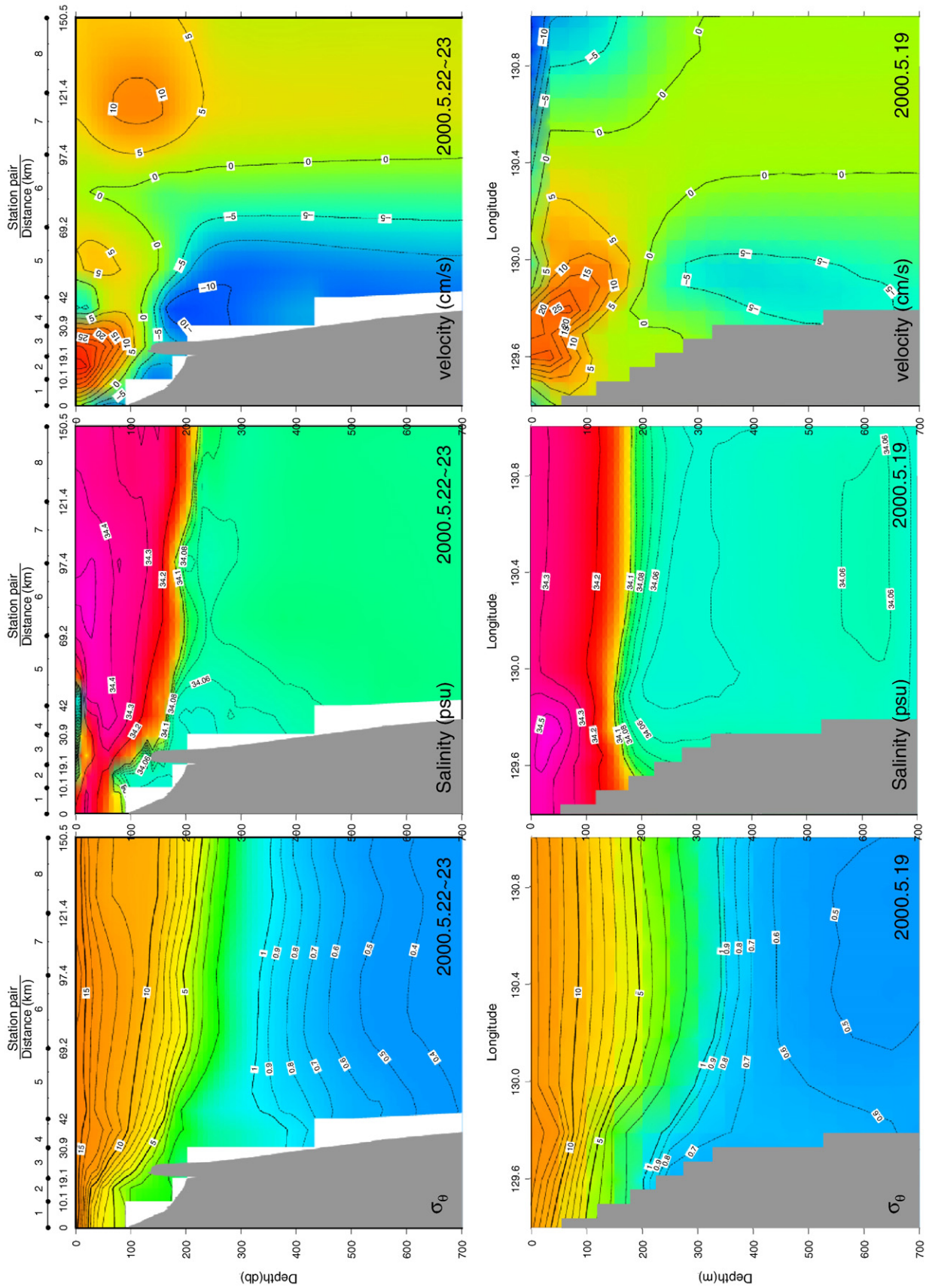
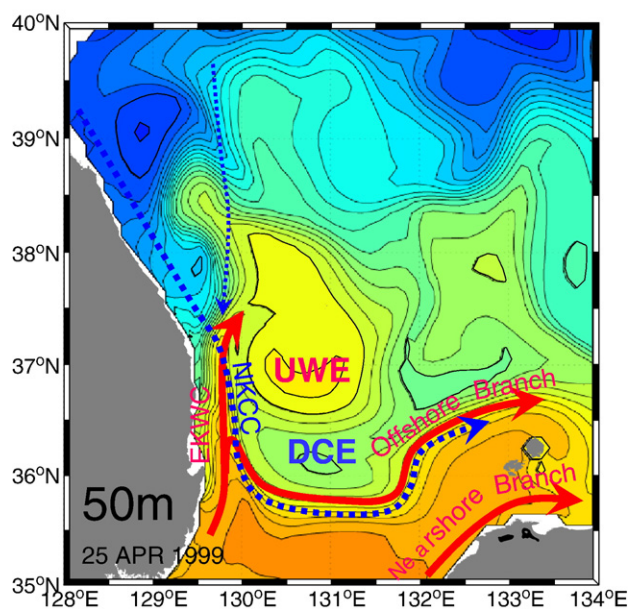


Fig. 15. Vertical sections of observed temperature, salinity and velocity across a zonal section HP close to line N, and simulated temperature, salinity and velocity across line N (lower panel) in May, 2000.



**Fig. 16.** Schematic of circulation pattern around the UB inferred from the reanalyzed products by the DA-ESROM in April, 1999. Color map and contour lines denote simulated SSH from high (red) to low (blue).

consider the flow-dependent and multi-variate background error covariance. We expect that it becomes more natural to assimilate the SSH into the ocean model and to consider the dynamically consistent assimilation system through the EnKF technique.

## 6. Uncited reference

Lim and Chang, 1969

## Acknowledgement

We are grateful to two anonymous reviewers for their valuable comments and suggestions. Special thanks are directed to Dr. M. Hofmann who kindly provided the SOM code. The altimeter products were produced by Ssalto/Duacs and distributed by Aviso, with support from Cnes. The major part of this work was conducted with financial support by Agency for Defense Development under the contract UD031003AD. The first and seventh authors were supported at the final stage of this work by KORDI's research projects (PE97701 and PG45100). The second author was supported by EAST-I Program of the Ministry of Maritime Affairs and Fisheries.

## References

- Bahurel, P., the MERCATOR Project Team, 2006. MERCATOR ocean global to regional ocean monitoring and forecasting. In: Chassignet, P., Verron, J. (Eds.), *Ocean Weather Forecasting: An Integrated View of Oceanography*. Springer, Netherlands, pp. 381–395.
- Bell, M.J., Barciela, R., Hines, A., Martin, M., Sellar, A., Storkey, D., 2006. The Forecasting Ocean Assimilation Model (FOAM) system. In: Chassignet, P., Verron, J. (Eds.), *Ocean Weather Forecasting: An Integrated View of Oceanography*. Springer, Netherlands, pp. 397–411.
- Budyko, M.I., 1974. *Climate and life*. International Geophysics Series, vol. 18. Academic Press, New York, 508 pp.
- Chang, K.-I., Hogg, N., Suk, M.-S., Byun, S.-K., Kim, Y.-G., Kim, K., 2002. Mean flow and variability in the southwestern East Sea. *Deep-Sea Res.* 49, 2261–2279.
- Chang, K.-I., Teague, W.J., Lyu, S.J., Perkins, H.T., Lee, D.-K., Watts, D.R., Kim, Y.-B., Mitchell, D.A., Lee, C.M., Kim, K., 2004. Circulation and currents in the southwestern East/Japan Sea: overview and review. *Prog. Oceanogr.* 61, 105–156.
- Cho, Y.-K., Kim, K., 1994. Two modes of the salinity minimum layer in the Ulleung Basin. *La Mer* 32, 271–278.
- Cho, Y.-K., Kim, K., 1996. Seasonal variation of the East Korean Warm Current and its relation with the cold water. *La Mer* 34, 172–182.

- Choi, B.H., Kim, K.O., Eum, H.M., 2002. Digital bathymetric and topographic data for neighboring seas of Korea. *J. Korean Soc. Coastal Ocean Eng.* 14, 41–50 (in Korean with English abstract).
- Cooper, M., Haines, K., 1996. Altimetric assimilation with water property conservation. *J. Geophys. Res.* 101 (C1), 1959–1977.
- Courtier, P., 1997. Dual formulation of four dimensional variational assimilation. *Q. J. R. Meteorol. Soc.* 123, 2449–2462.
- Derber, J., Bouttier, F., 1999. A reformulation of the background error covariance in the ECMWF global data assimilation system. *Tellus* 51A, 195–221.
- Evensen, G., 1994. Sequential data assimilation with a nonlinear quasi-geostrophic model using Monte Carlo methods to forecast error statistics. *J. Geophys. Res.* 99, 10143–10162.
- Griffies, S.M., Pacanowski, R.C., Schmidt, M., Balaji, V., 2001. Tracer conservation with an explicit free surface method for z-coordinate ocean models. *Mon. Weather Rev.* 129, 1081–1098.
- Hirose, Naoki, Fukumori, I., Yoon, J.-H., 1999. Assimilation of TOPEX/POSEIDON altimeter data with a reduced gravity model of the Japan Sea. *J. Oceanogr.* 55 (1), 53–64.
- Hofmann, M., Maqueda, M.A.M., 2006. Performance of a second-order moments advection scheme in an Ocean General Circulation Model. *J. Geophys. Res.* 111, C05006. doi:10.1029/2005JC003279.
- Ichiye, T., Takano, K., 1988. Mesoscale eddies in the Sea of Japan. *La Mer* 26, 69–79.
- Ishikawa, Y., Awaji, T., Toyoda, T., In, T., Nishina, K., Nakayama, T., Shima, S., 2007. High-resolution synthetic monitoring by a 4-dimensional variational data assimilation system in the northwestern North Pacific. *J. Geophys. Res.* 112, C07004. doi:10.1029/2006JC004004.
- Kawabe, M., 1982a. Branching of the Tsushima Current in the Japan Sea. Part I. Data analysis. *J. Oceanogr. Soc. Japan* 38, 95–107.
- Kawabe, M., 1982b. Branching of the Tsushima Current in the Japan Sea. Part II. Numerical experiment. *J. Oceanogr. Soc. Japan* 38, 183–192.
- Kawamura, H., Wu, P., 1998. Formation mechanism of the Japan Sea Proper water in the flux center off Vladivostok. *J. Geophys. Res.* 103, 611–622.
- Kim, K., Chung, J.Y., 1984. On the salinity-minimum and dissolved oxygen maximum layer in the East Sea (Sea of Japan). In: Ichiye, T. (Ed.), *Ocean Hydrodynamics of the Japan and East China Seas*. Elsevier, New York, pp. 56–66.
- Kim, C.H., Kim, K., 1983. Characteristics and origin of the cold water mass along the east coast of Korea. *J. Oceanol. Soc. Korea* 18, 73–83 (in Korean).
- Kim, Y.-G., Kim, K., 1999. Intermediate waters in the East/Japan Sea. *J. Oceanogr.* 55, 123–132.
- Kim, C.-H., Yoon, J.-H., 1999. A numerical modeling of the upper and the intermediate layer circulation in the East Sea. *J. Oceanogr.* 55, 327–345.
- Kim, K., Lyu, S.J., Kim, Y.-G., Choi, B.H., Taira, K., Perkins, H.T., Teague, W.J., Book, J.W., 2004. Monitoring Volume Transport through Measurement of Cable Voltage across the Korea Strait. *J. Atmos. Ocean. Technol.* 21 (4), 671–682.
- Large, W.G., McWilliams, J.C., Doney, S.C., 1994. Oceanic vertical mixing: a review and a model with a nonlocal boundary layer parameterization. *Rev. Geophys.* 32, 363–403.
- Large, W.G., Danabasoglu, G., Doney, S.C., McWilliams, J.C., 1997. Sensitivity to Surface Forcing and Boundary Layer Mixing in a Global Ocean Model. *J. Phys. Oceanogr.* 27, 2418–2447.
- Lee, H.J., Yoon, J.-H., Kawamura, H., Kang, H.-W., 2003. Comparison of RIAMOM and MOM in Modeling the East Sea/Japan Sea Circulation. *Ocean Polar Res.* 25 (3), 287–302.
- Lim, D.B., Chang, S., 1969. On the cold water mass in the Korea Strait. *J. Oceanol. Soc. Korea* 4, 71–82.
- Marchesello, P., McWilliams, J.C., Shchepetkin, A., 2001. Open boundary conditions for long-term integration of regional oceanic models. *Ocean Model.* 3, 1–20.
- Mitchell, D.A., Watts, D.R., Wimbush, M., Teague, W.J., Tracey, K.L., Book, J.W., Chang, K.-I., Suk, M.-S., Yoon, J.-H., 2005a. Upper circulation patterns in the Ulleung Basin. *Deep-Sea Res.* 52, 1617–1638.
- Mitchell, D.A., Teague, W.J., Wimbush, M., Watts, D.R., Sutyrin, G.G., 2005b. The Dok Cold Eddy. *J. Phys. Oceanogr.* 35, 273–288.
- Na, J.Y., Seo, J.W., 1998. The sea surface winds and heat flux in the East Asian Marginal Seas. The Report at Department of Earth and Marine Sciences. HanYang University, Korea. 52 pp.
- Na, J.Y., Seo, J.W., Han, S.K., 1992. Monthly mean sea surface winds over the adjacent seas of the Korea Peninsula. *J. Oceanol. Soc. Korea* 27, 1–10.
- Na, Hanna, Isoda, Y., Kim, K., Kim, Y.H., Lyu, S.J., 2007. Recent observation of hydrography, currents and volume transport in the straits of the East/Japan Sea: a review. *J. Geophys. Res.* 112, C07004. doi:10.1029/2006JC004004.
- Nam, S.H., Lyu, S.J., Kim, Y.H., Kim, K., Park, J.-H., Watts, D.R., 2004. Correction of TOPEX/POSEIDON altimeter data for nonisostatic sea level response to atmospheric pressure in the Japan/East Sea. *J. Geophys. Res. Lett.* 31, L02304. doi:10.1029/2003GL018487.
- Nam, S.H., Lyu, S.J., Kim, Y.H., Kim, K., 2005. Corrections of altimetry data for nonisostatic sea level response to atmospheric pressure in the East (Japan) Sea. *Proceedings of 25th Anniversary IGARSS 2005*, p. 5412.
- Pacanowski, R.C., Gnanadesikan, A., 1998. Transient response in a z-level ocean model that resolves topography with partial-cells. *Mon. Weather Rev.* 126 (12), 3248–3270.
- Pacanowski, R.C., Griffies, S.M., 1999. MOM3.0 Manual. WWW Page, [http://www.gfdl.noaa.gov/~smg/MOM/web/guide\\_parent/guide\\_parent.html](http://www.gfdl.noaa.gov/~smg/MOM/web/guide_parent/guide_parent.html).
- Park, K.-A., Chung, J.Y., Kim, K., 2004. Sea surface temperature fronts in the East (Japan) Sea and temporal variations. *J. Geophys. Res. Lett.* 31, L07304. doi:10.1029/2004GL019424.
- Prather, M.J., 1986. Numerical advection by conservation of second-order moments. *J. Geophys. Res.* 91, 6671–6681.
- Roberts, M., Marshall, D., 1998. Do we require adiabatic dissipation schemes in eddy-resolving ocean models? *J. Phys. Oceanogr.* 28, 2050–2063.

- 766 Smagorinsky, J., 1993. Some historical remarks on the use of nonlinear viscosities. In:  
767 Galperin, B., Orszag, S.A. (Eds.), Large eddy simulation of complex engineering and  
768 geophysical flows. Cambridge University Press, Cambridge, UK, pp. 2–36.
- 769 Troen, I.B., Mahrt, L., 1986. A simple model of the atmospheric boundary layer;  
770 sensitivity to surface evaporation. *Boundary-Layer Meteorol.* 37, 129–148.
- 771 Weaver, A., Courtier, P., 2001. Correlation modeling on the sphere using a generalizing  
772 diffusion equation. *Q. J. R. Meteorol. Soc.* 127, 1815–1846.
- 773 Yoon, J.-H., 1982a. Numerical experiment on the circulation in the Japan Sea. Part II.  
774 Influence of seasonal variations in atmospheric conditions on the Tsushima  
775 Current. *J. Oceanogr. Soc. Japan* 38, 81–94.
- Yoon, J.-H., 1982b. Numerical experiment on the circulation in the Japan Sea. Part III. 776  
Mechanism of the nearshore branch of the Tsushima Current. *J. Oceanogr. Soc.* 777  
*Japan* 38, 125–130. 778
- Yoon, J.-H., Kawamura, H., 2002. The formation and circulation of the intermediate 779  
water in the Japan Sea. *J. Oceanogr.* 58, 197–211. 780
- Yoon, J.-H., Kim, Y.-J., 2007-this issue. The seasonal variation of the surface circulation of 781  
the Japan/East Sea and roles of meso- and submeso-scale variabilities. 782
- Yoshikawa, Y., Awaji, T., Akitomo, K., 1999. Formation and circulation processes of 783  
intermediate water in the Japan Sea. *J. Phys. Oceanogr.* 29, 1701–1722. 784  
785

UNCORRECTED PROOF